

## 1 **Paleoclimate evidence of vulnerable permafrost during times of low sea ice**

2 Vaks, A.\*, Mason, A. J., Breitenbach, S. F. M., Kononov, A. M., Osinzev, A. V., Rosensaft, M.,  
3 Borshevsky, A., Gutareva, O. S., and Henderson, G. M.

4 **Climate change in the Arctic is occurring rapidly, and projections suggest the complete loss of**  
5 **summer sea-ice by the middle of this century<sup>1</sup>. The sensitivity of permanently frozen ground**  
6 **(permafrost) in the Northern Hemisphere to warming is less clear, and long-term trends are harder**  
7 **to monitor than those of sea-ice. Here we use paleoclimate data to indicate that Siberian permafrost**  
8 **is robust to warming when Arctic sea-ice is present, but vulnerable when it is absent. U-Pb**  
9 **chronology of carbonate deposits (speleothems) in a Siberian cave located at the southern edge of**  
10 **continuous permafrost, reveal periods when the overlying ground was not permanently frozen. The**  
11 **speleothem record starts 1.5 million years ago (Ma), a time when greater equator-to-pole heat**  
12 **transport led to a warmer northern hemisphere<sup>2</sup>. Speleothems' growth demonstrate that permafrost**  
13 **at the cave site was absent at this time, becoming more common from  $\approx 1.35$  Ma as the Northern**  
14 **Hemisphere cooled, and permanent after  $\approx 0.4$  Ma. This history mirrors that of year-round sea-ice in**  
15 **the Arctic Ocean, which was largely absent prior to  $\approx 0.4$  Ma<sup>3</sup>, but continuous since that date. The**  
16 **robustness of permafrost when sea-ice is present, and increased permafrost vulnerability when sea-**  
17 **ice is absent can be explained by changes in both heat and moisture transport. Reduced sea-ice may**  
18 **contribute to warming of Arctic air<sup>4-6</sup> that can lead to warming far inland<sup>7</sup>. Open Arctic waters also**  
19 **increase the source of moisture and increase autumn snowfall over Siberia, insulating the ground**  
20 **from cold winter temperatures<sup>8-10</sup>. These processes explain the relationship between an ice-free Arctic**  
21 **and permafrost thawing prior to 0.4 Ma. If these processes continue during modern climate change,**  
22 **future loss of summertime Arctic sea-ice will enhance thawing of Siberian permafrost.**

23 Arctic Ocean sea-ice declined increasingly rapidly in recent decades, with progressive ice thinning and  
24 increasing areas of open water during the summer-time<sup>11</sup>. Complete loss of summer sea-ice is expected by

25 the mid-21st century<sup>1</sup>. The recent loss of Arctic sea-ice raises concerns about its effects on other aspects of  
26 the global climate system, including potential acceleration of permafrost thawing<sup>7</sup>. Permafrost degradation  
27 as a result of anthropogenic global warming could amplify the climate change by releasing large volumes  
28 of carbon stored in permafrost in the form of CO<sub>2</sub> and methane<sup>12</sup>. In addition, permafrost thawing increases  
29 thermokarst development, coastal erosion, and liquefaction of ground previously cemented by ground ice,  
30 endangering infrastructures relying on permafrost as solid ground<sup>13</sup>. Establishing the relationship between  
31 loss of Arctic sea-ice and permafrost response is therefore an important goal.

32 Understanding of the response of permafrost to changing climate can be improved with knowledge of past  
33 environmental conditions. Precisely dated growth periods of speleothems (stalagmites, stalactites and  
34 flowstones) from caves located in permafrost regions have proved an effective tool for reconstruction of  
35 past permafrost extent and continuity<sup>14</sup>. Speleothems grow only when meteoric waters seep through the  
36 vadose zone into caves. When temperature in the upper vadose zone falls below 0°C throughout the year,  
37 water freezes, infiltration stops, and speleothem growth ceases. Speleothems found in modern permafrost  
38 regions are thus relicts from warmer periods when permafrost was absent, or when permafrost thawed  
39 temporarily<sup>14,15</sup>. Dating of these relicts allow comparison of periods of permafrost absence to other aspects  
40 of past environment.

41 In this study we reconstruct permafrost dynamics in central Eastern Siberia over the last 1,500 ka, using U-  
42 Pb dated speleothems from Ledianaya Lenskaya Cave (60°22'15.60"N-116°56'47.30"E) (Fig. 1) located  
43 in the zone of present-day continuous permafrost (i.e., year-round frozen ground across the whole region<sup>16</sup>,  
44 Extended Data (ED) 3). The study area is characterized by cold continental climate (Dfc according to the  
45 Köppen classification<sup>17</sup>), with mean July and January air temperatures of +18°C and -32°C respectively,  
46 and a mean annual air temperature (MAAT) of ~-6°C (ED 2), while annual precipitation is ~400 mm. The  
47 record from Ledianaya Lenskaya Cave is compared with data from Botovskaya Cave (55°17'59.03"N-  
48 105°19'46.02"E) (Fig. 1), located in an area of discontinuous permafrost and MAAT of ~-2°C (ED 2, 3).

49 This study continues the research of Vaks et al (2013)<sup>14</sup> which found that, in Ledyanaya Lenskaya Cave,  
50 the most recent permafrost thaw occurred at  $429 \pm 23 \text{ ka}^i$ <sup>18</sup>, during the warmth of Marine Isotopic Stage  
51 (MIS) 11<sup>19</sup>. That study was limited, however, by the ~500 ka range of U-Th chronology, meaning that older  
52 samples could not be analyzed. U-Pb chronology enables dating of such older speleothems. Here we use  
53 52 U-Pb ages on 11 speleothems from Ledyanaya Lenskaya Cave to greatly extend the age range of known  
54 Siberian permafrost history. A smaller number of ages were also determined on three samples from the  
55 more southerly and warmer Botovskaya Cave<sup>14</sup> (Fig. 1) (see Methods, ED, and Data Tables 1 and 2 – for  
56 chronological methods and full results). Ages indicate a division of speleothem deposition in Ledyanaya  
57 Lenskaya Cave, and therefore of permafrost presence, into three distinct periods (Figs. 2A, 3A):

58 During the period from **1,500 to ~1,350 ka** speleothems apparently grew continuously (within the limits  
59 of analytical uncertainties), suggesting discontinuous or absent permafrost above the cave. Globally, this  
60 interval spans MIS-50 to MIS-43 and is characterized by glacial-interglacial cycles with 41 ky  
61 periodicity<sup>19</sup>. Most of the analyzed speleothems in Ledyanaya Lenskaya Cave grew in this period (7 out  
62 of 11) (ED 4). These oldest vadose speleothems were the first deposited directly on the cave host-rock,  
63 heralding the onset of vadose conditions at this site, and suggesting that, before 1,500 ka, the cave may  
64 have been located below the local groundwater level. The current groundwater table is located ~50 m  
65 below the cave's entrance and controlled by the nearby Lena River.

66 The period from **~1,350 to ~400 ka** is defined by intermittent speleothem growth with long-lasting hiatuses  
67 without speleothem deposition. These growth cessations are likely to indicate continuous periods of  
68 permafrost and are found at the time of most glacial MISs and some interglacial MISs. Speleothem growth,  
69 demonstrating the absence of permafrost, occurred during most interglacials (Fig. 2A). Since ~1,300 ka  
70 speleothems only grew in the shallower portion of the cave (15-20 m below the surface) and not in the  
71 deeper area (~60 m) (Fig. 2A, 3A; ED 1). This may indicate that the permafrost was thawing only to depth

---

<sup>i</sup> The original age cited by Vaks et al (2013) is  $427 \pm 23 \text{ ka}$ , the age above is re-calculated using updated half-lives of <sup>234</sup>U and <sup>230</sup>Th<sup>18</sup>

72 of 15-20 m, whereas relict permafrost remained at greater depth, showing that the duration of thawing  
73 periods was relatively short and/or that MAAT were reduced compared to the period prior to 1,300 ka.

74 ***From ~400 ka until present*** speleothem growth ceased completely and permafrost appears to have been  
75 continuous above Ledianaya Lenskaya Cave (Fig. 2A, 3A and ED)<sup>14</sup>.

76 Caves located further south near Lake Baikal (Botovskaya and Okhotnichya) (Fig. 1) show speleothem  
77 deposition during warm periods during the last 700 ka (this study, and Vaks et al (2013)<sup>14</sup> (Fig. 2A and  
78 ED)). These southerly caves indicate that climate in southern Siberia was warmer than in Ledianaya  
79 Lenskaya Cave, enabling deposition of speleothems, while in Ledianaya Lenskaya Cave to the north  
80 speleothem growth ceased completely for the entire last ~400 ka.

81 Based on data for the last 500 ka, Vaks et al (2013)<sup>14</sup> found permafrost thawing at Ledianaya Lenskaya  
82 Cave during the unusual warmth of MIS-11 (429±23 ka) but not in younger interglacials. They suggested  
83 that an increase in global mean surface temperature of 1.5°C (above preindustrial levels) represents the  
84 threshold above which continuous permafrost thaws at its southern fringes. Our new results indicate that  
85 substantial speleothem deposition occurred prior to MIS-11, when global mean surface temperatures (as  
86 indicated by Pacific Warm Pool sea-surface-temperatures) were lower than those of MIS-11 (e.g. MIS 25,  
87 19, 15), and even lower than today (e.g. MIS 23, Fig. 2C)<sup>20</sup>. These earlier periods of speleothem growth  
88 indicate that global mean surface temperature is not the only control on the extent of Siberian permafrost.  
89 Other possible controls may include: 1) local summer insolation; 2) paleo-geographic changes; 3) greater  
90 poleward heat transport in the Northern hemisphere, leading to relatively warmer conditions in the North  
91 Atlantic, Arctic, and/or over the Eurasian landmass; or 4) Arctic Ocean sea-surface temperatures (SST) and  
92 the extent of Arctic summer sea-ice cover.

93 The intensity of summer insolation on latitude 60°N (Fig. 2D)<sup>21</sup> may directly affect Siberian summer  
94 temperatures and therefore influence permafrost thawing. Many periods of speleothem deposition occurred  
95 when July insolation was high (i.e. >500 W/m<sup>2</sup>), but there is no direct relationship between insolation and

96 thawing of permafrost. No thawing took place during periods of insolation  $>500 \text{ w/m}^2$  during the last 400  
 97 ka, but thawing did occur at much lower insolation earlier in the record. Local summer insolation is  
 98 therefore not the key factor determining the presence of permafrost above Ledyanaya Lenskaya Cave.

99 Arctic paleogeographic conditions during *interglacials* of the entire last 1,500 ka were similar to present,  
 100 with the open Bering Strait, enabling water exchange between Pacific and Arctic oceans<sup>22</sup>. The Atlantic  
 101 Meridional Overturning Circulation (AMOC) transports heat from the tropics to the northern Atlantic  
 102 Ocean thereby increasing the heat flux to high latitudes in continental Eurasia and the Arctic<sup>23</sup>. The period  
 103 between ~2.4 and 1.3 Ma was characterized by enhanced AMOC, causing heat piracy from the southern to  
 104 the northern hemisphere, which was consequently relatively warm<sup>2</sup>. This enhanced northward heat flux  
 105 caused significantly warmer SSTs in the North Atlantic than those of most of Middle-Late Quaternary and  
 106 Holocene<sup>2</sup> (Fig. 3C, D). After ~1,300 ka the AMOC gradually weakened, leading to concurrent lowering  
 107 of North Atlantic SST of  $1.5^\circ\text{C}$  to  $3^\circ\text{C}$ <sup>24</sup> (Fig. 3C, D). This is likely to cause progressive cooling of the  
 108 Eurasian landmass on long-term scale and could influence the presence of permafrost (which is much less  
 109 common early in the record when the northern hemisphere was warmer on average). Again, there is no  
 110 simple relationship between speleothem growth in Ledyanaya Lenskaya Cave and North Atlantic warmth:  
 111 periods of significant North Atlantic warmth during the last 400 ka are not associated with permafrost  
 112 thawing. For example: MIS-9 (Fig. 3C, D) and MIS-5 (Fig. 3D) were warmer than all other times in the  
 113 last ~1,300 ka, but there is no permafrost thawing above Ledyanaya Lenskaya Cave. Of these, MIS-5 is  
 114 particularly notable because both the Pacific Warm Pool (Fig. 2C) and North Atlantic (Fig. 3D) were  
 115 warmer than many earlier thaw periods, and as warm as interglacials in the period of 1,500-1,300 ka when  
 116 the permafrost above the Ledyanaya Lenskaya Cave was discontinuous or absent. Yet, there is no evidence  
 117 for permafrost thawing above Ledyanaya Lenskaya Cave at MIS-5 (Fig. 3A).

118 It is striking that the permanent presence of permafrost since 400 ka initiates at the same time as perennial  
 119 sea-ice is established in the Arctic Ocean (Fig. 3A, 3E). The appearance of perennial sea-ice is marked by  
 120 an abrupt increase in the appearance of sea-ice-associated fauna in the western Arctic Ocean<sup>3</sup> (Fig.3E) and

121 the disappearance from the Arctic Ocean of fauna that today is found in the North Atlantic<sup>25</sup>. The perennial  
122 Arctic sea-ice (Fig. 3E) remained intact even during MIS-9 and MIS-5e, when both the tropics (Fig. 2C)  
123 and North Atlantic (Fig. 3C, D) were particularly warm.

124 Climatic models for present and past climates indicate a relationship between Arctic sea-ice and Eurasian  
125 permafrost caused by changes in atmospheric heat transport<sup>5,26</sup>. Removal of Arctic sea-ice warms the air  
126 above the sea surface<sup>5</sup>, increasing the moisture content of the atmosphere, and therefore increasing the  
127 transport of both sensible and latent heat from the ocean via atmospheric transport to continental interiors<sup>4</sup>.  
128 Resulting warming can penetrate up to 1,500 km inland, peaking in autumn, and leading to permafrost  
129 degradation<sup>7</sup>. An open Arctic Ocean also leads directly to increased transport of moisture from the sea to  
130 the continent. High d-excess values of autumn atmospheric precipitation in Siberia show that open Arctic  
131 Ocean comprises a substantial moisture source that is shut down when the Arctic ice cover is established  
132 in early winter<sup>27</sup>. Models show that future increase in Arctic precipitation will come mainly from  
133 evaporation from Arctic Ocean due to retreating sea-ice, and not from enhanced moisture transport from  
134 lower latitudes<sup>28</sup>. At present, decreased sea-ice cover in the autumn increases moisture and leads to heavier  
135 autumn snowfall over Siberia<sup>8,9</sup>. Thicker autumn snow cover insulates the ground from cold winter  
136 temperatures, increasing winter and mean annual ground temperatures<sup>9,10</sup>. This effect, well known to  
137 influence seasonal vegetation<sup>10</sup>, has not previously been recognized as a significant long-term control on  
138 the extent of permafrost, but the strong relationship between perennial sea-ice and permafrost observed in  
139 this study suggests it may be an important controlling factor. The appearance of perennial sea-ice 400 ka  
140 ago decreases the Arctic heat (sensible and latent) and moisture source<sup>27</sup> cooling the Arctic air and reducing  
141 snowfall on the continent. That may lead to poorer ground insulation and lowering of ground temperature,  
142 assisting to the establishment of continuous permafrost<sup>29</sup>. Future loss of summer sea-ice may have the  
143 opposite effect, warming ground temperatures and speeding the thawing of permafrost.

144 The stability of continuous permafrost near its modern southern boundary in Siberia hinges on perennial  
145 sea-ice cover in the Arctic Ocean. Although the speleothems' record of this study also indicates intervals

146 of permafrost prior to the formation of perennial sea-ice on ~400 ka, such permafrost was prone to  
147 thawing in times of higher Northern Atlantic and/or global mean temperature. The long-term cooling of  
148 Arctic Ocean that occurred between ~1,350 ka and ~400 ka eventually reached a temperature threshold  
149 for the formation of perennial Arctic sea-ice, which stabilized the presence of continuous permafrost in  
150 Siberian regions where it remains today. This new record indicates that, under future open-water Arctic  
151 scenarios as predicted for later this century<sup>30</sup>, this stabilization is likely to be removed, enhancing the  
152 northerly retreat of continuous permafrost.

### 153 **Acknowledgments**

154 We would like to thank Kazanzev, I. G., Stol'arov, V. A., Sokol'nikov, D. S., and other Speleoclub  
155 Arabica members for their help with expeditions' organizations, mapping the caves and collecting  
156 samples. We would like to thank Alexeev, S. V., Kozireva, E. A., Pellinen, V. A., and Svetlakov, A. A.,  
157 from Institute of Earth's Crust of the Russian Academy of Sciences (IEC RAS) in Irkutsk for help in the  
158 field and with samples shipment. We thank Balaev, V. A. and Alexioglo, V. V., from Lensk, for their help  
159 during the fieldwork in Ledianaya Lenskaya Cave. We thank Kwiecien, O. from Ruhr University  
160 Bochum, Germany, Lechleitner, F. from University of Oxford, UK, and Brall, N. from University of  
161 Lyon, France, for help with samples collecting in Botovskaya Cave, We thank Cohen, B. from Geological  
162 Survey of Israel for the help with graphic work. We thank Schirrmeister, L., Parrish, R., and third  
163 anonymous reviewer for useful comments that helped to substantially improve the quality of this paper.  
164 We also gratefully acknowledge the NOAA Air Resources Laboratory (ARL) for the provision of the  
165 HYSPLIT transport and dispersion model and/or READY website (<https://www.ready.noaa.gov>) used in  
166 this publication. This work was funded by NERC Fellowship NE/G013829/1, NERC Standard Grant  
167 NE/K005057/1, Royal Society grant JP080831 and RFBR joint grant 09-05-92605 KO\_a.

### 168 **Author contributions:**

169 A.V., G.M.H. and S.F.M.B. devised the approach of using caves to reconstruct permafrost, and raised the  
 170 funding for this research. A.V., A.V.O., S.F.M.B., and O.S.G. conducted the field work, with help from  
 171 A.M.K.. A.J.M. led the development and application of the chronological work, with input from A.V. and  
 172 G.M.H.. A.V.O., M.R., A.B., S.F.M.B. and A.M.K. drew the maps (permafrost and caves) with input  
 173 from all authors. A.V. led the interpretation of the data, and the writing of the manuscript, with input from  
 174 all authors.

## 175 References:

- 176 1 IPCC, 2013: Climate Change 2013: The Physical Science Basis. Contribution of Working Group I to  
 177 the Fifth Assessment Report of the Intergovernmental Panel on Climate Change. 1535 pp  
 178 (Cambridge University Press, Cambridge, United Kingdom and New York, NY, USA, 2013).
- 179 2 Bell, D. B., Jung, S. J. A. & Kroon, D. The Plio-Pleistocene development of Atlantic deep-water  
 180 circulation and its influence on climate trends. *Quaternary Science Reviews* **123**, 265-282,  
 181 doi:<http://dx.doi.org/10.1016/j.quascirev.2015.06.026> (2015).
- 182 3 Cronin, T. M. *et al.* Enhanced Arctic Amplification Began at the Mid-Brunhes Event ~400,000  
 183 years ago. *Scientific Reports* **7**, 14475, doi:10.1038/s41598-017-13821-2 (2017).
- 184 4 Ballantyne, A. P. *et al.* The amplification of Arctic terrestrial surface temperatures by reduced  
 185 sea-ice extent during the Pliocene. *Palaeogeography, Palaeoclimatology, Palaeoecology* **386**, 59-  
 186 67, doi:<https://doi.org/10.1016/j.palaeo.2013.05.002> (2013).
- 187 5 Dai, A., Luo, D., Song, M. & Liu, J. Arctic amplification is caused by sea-ice loss under increasing  
 188 CO<sub>2</sub>. *Nature Communications* **10**, 121, doi:10.1038/s41467-018-07954-9 (2019).
- 189 6 Screen, J. A. & Simmonds, I. The central role of diminishing sea ice in recent Arctic temperature  
 190 amplification. *Nature* **464**, 1334, doi:10.1038/nature09051  
 191 <https://www.nature.com/articles/nature09051#supplementary-information> (2010).
- 192 7 Lawrence, D. M., Slater, A. G., Tomas, R. A., Holland, M. M. & Deser, C. Accelerated Arctic land  
 193 warming and permafrost degradation during rapid sea ice loss. *Geophysical Research Letters*  
 194 **35**, 1-6 (2008).
- 195 8 Liu, J., Curry, J. A., Wang, H., Song, M. & Horton, R. M. Impact of declining Arctic sea ice on  
 196 winter snowfall. *Proceedings of the National Academy of Sciences*,  
 197 doi:10.1073/pnas.1114910109 (2012).
- 198 9 Park, H., Walsh, J. E., Kim, Y., Nakai, T. & Ohata, T. The role of declining Arctic sea ice in recent  
 199 decreasing terrestrial Arctic snow depths. *Polar Science* **7**, 174-187,  
 200 doi:<https://doi.org/10.1016/j.polar.2012.10.002> (2013).
- 201 10 Zhang, T. Influence of the seasonal snow cover on the ground thermal regime: An overview.  
 202 *Reviews of Geophysics* **43**, doi:10.1029/2004RG000157 (2005).
- 203 11 Serreze, M. C. & Stroeve, J. Arctic sea ice trends, variability and implications for seasonal ice  
 204 forecasting. *Philosophical Transactions of the Royal Society A: Mathematical, Physical and*  
 205 *Engineering Sciences* **373**, doi:10.1098/rsta.2014.0159 (2015).
- 206 12 Schuur, E. A. G. *et al.* Vulnerability of Permafrost Carbon to Climate Change: Implications for the  
 207 Global Carbon Cycle. *BioScience* **58**, 701-714, doi:10.1641/b580807 (2008).



208 13 Anisimov, O. & Reneva, S. Permafrost and Changing Climate: The Russian Perspective. *AMBIO: A*  
209 *Journal of the Human Environment* **35**, 169-175, doi:10.1579/0044-  
210 7447(2006)35[169:pacctr]2.0.co;2 (2006).  
211 14 Vaks, A. *et al.* Speleothems Reveal 500,000-Year History of Siberian Permafrost. *Science* **340**  
212 183-186, doi:10.1126/science.1228729 (2013).  
213 15 Lauriol, B., Ford, D. C., Cinq-Mars, J. & Morris, W. A. The chronology of speleothem deposition in  
214 northern Yukon and its relationships to permafrost. *Canadian Journal of Earth Sciences* **34**, 902-  
215 911, doi:10.1139/e17-075 (1997).  
216 16 Brown, J., Ferrians, J. O. J., Heginbottom, J. A. & Melnikov, E. S. in *Circum-Arctic map of*  
217 *permafrost and ground-ice conditions, in Circum-Pacific Map Series CP-45, scale 1:10,000,000*  
218 (US Geological Survey in Cooperation with the Circum-Pacific Council for Energy and Mineral  
219 Resources., Washington, DC: U.S., 1997).  
220 17 Peel, M. C., Finlayson, B. L. & McMahon, T. A. Updated world map of the Köppen-Geiger climate  
221 classification. *Hydrology and Earth System Sciences Discussions, European Geosciences Union* **11**,  
222 1633-1644 (2007).  
223 18 Cheng, H. *et al.* Improvements in <sup>230</sup>Th dating, <sup>230</sup>Th and <sup>234</sup>U half-life values, and U–Th  
224 isotopic measurements by multi-collector inductively coupled plasma mass spectrometry. *Earth*  
225 *and Planetary Science Letters* **371-372**, 82-91, doi:https://doi.org/10.1016/j.epsl.2013.04.006  
226 (2013).  
227 19 Lisiecki, L. E. & Raymo, M. E. A Pliocene-Pleistocene stack of 57 globally distributed benthic  $\delta^{18}\text{O}$   
228 records *Paleoceanography* **20**, doi:10.1029/2004PA001071 (2005).  
229 20 Hansen, J. *et al.* Global temperature change. *Proceedings of the National Academy of Sciences*  
230 **103**, 14288-14293, doi:10.1073/pnas.0606291103 (2006).  
231 21 Laskar, J. *et al.* A long-term numerical solution for the insolation quantities of the Earth.  
232 *Astronomy and Astrophysics* **428**, 261-285, doi: 10.1051/0004-6361:20041335 (2004).  
233 22 Kender, S. *et al.* Closure of the Bering Strait caused Mid-Pleistocene Transition cooling. *Nature*  
234 *Communications* **9**, 5386, doi:10.1038/s41467-018-07828-0 (2018).  
235 23 Maroon, E. A., Kay, J. E. & Karnauskas, K. B. Influence of the Atlantic Meridional Overturning  
236 Circulation on the Northern Hemisphere Surface Temperature Response to Radiative Forcing.  
237 *Journal of Climate* **31**, 9207-9224, doi:10.1175/jcli-d-17-0900.1 (2018).  
238 24 Lawrence, K. T., Sosdian, S., White, H. E. & Rosenthal, Y. North Atlantic climate evolution  
239 through the Plio-Pleistocene climate transitions. *Earth and Planetary Science Letters* **300**, 329-  
240 342, doi:<http://dx.doi.org/10.1016/j.epsl.2010.10.013> (2010).  
241 25 Cronin, T. M. *et al.* Quaternary ostracode and foraminiferal biostratigraphy and  
242 paleoceanography in the western Arctic Ocean. *Marine Micropaleontology* **111**, 118-133,  
243 doi:https://doi.org/10.1016/j.marmicro.2014.05.001 (2014).  
244 26 Vandenberghe, J. *et al.* Eurasian permafrost instability constrained by reduced sea-ice cover.  
245 *Quaternary Science Reviews* **34**, 16-23, doi:https://doi.org/10.1016/j.quascirev.2011.12.001  
246 (2012).  
247 27 Kurita, N. Origin of Arctic water vapor during the ice-growth season. *Geophysical Research*  
248 *Letters* **38**, doi:10.1029/2010gl046064 (2011).  
249 28 Bintanja, R. & Selten, F. M. Future increases in Arctic precipitation linked to local evaporation  
250 and sea-ice retreat. *Nature* **509**, 479, doi:10.1038/nature13259 (2014).  
251 29 O'Neill, H. B. & Burn, C. R. Impacts of variations in snow cover on permafrost stability, including  
252 simulated snow management, Dempster Highway, Peel Plateau, Northwest Territories. *Arctic*  
253 *Science* **3**, 150-178, doi:10.1139/as-2016-0036 (2017).

Barnhart, K. R., Miller, C. R., Overeem, I. & Kay, J. E. Mapping the future expansion of Arctic open water. *Nature Climate Change* **6**, 280, doi:10.1038/nclimate2848 <https://www.nature.com/articles/nclimate2848#supplementary-information> (2015).

# **Figure captions:**

**Figure 1: Study area and permafrost maps.** (A) Permafrost map of northern Eurasia with the research area marked by the black rectangle, continuous permafrost in purple, discontinuous permafrost in green, and the area with no permafrost in yellow; (B) Extent of permafrost types in eastern Siberia<sup>16</sup> and the location of Ledianaya Lenskaya, Botovskaya and Okhotnichya caves, marked by black stars. Cities and towns are marked by grey circles. Permafrost types (see legend) are defined by the percentage of the year-round frozen ground.

**Figure 2: Siberian speleothem deposition periods compared to records of MIS, Pacific warm pool SSTs and July mean insolation on 60°N.** (A) Distribution of speleothem U-Pb and U-Th ages ( $\pm 2\sigma$ ) in Ledianaya Lenskaya Cave (purple circles) and in Botovskaya Cave (light blue circles at) in time (ka) and space (latitude °N). Ages of Ledianaya Lenskaya SLL14 speleothems (60 m below the surface) are marked by dark purple circles, and of SLL9/SLL10 speleothems (15-20 m below the surface) by light purple circles. Purple vertical rectangles show how periods of speleothem growth in Ledianaya Lenskaya Cave relate to other climatic records. (B) Benthic  $\delta^{18}\text{O}$  stack<sup>19</sup> with glacial MIS numbers below and interglacial above; (C) Pacific Warm Pool Mg/Ca inferred SST changes during the last 1400 ka, which are considered to be a reasonable reflection of changes in mean Earth surface temperature<sup>20</sup>. The preindustrial SST is marked by lower dotted red horizontal line and abbreviation “PI-SST”. The SST 1.5°C higher than preindustrial level is marked by upper dotted red line and abbreviation “+1.5°C-SST”; (D) July mean insolation at 60°N<sup>21</sup>.

**Figure 3: Siberian speleothem deposition periods compared to records of MIS, North Atlantic SST and presence of sea-ice in Arctic Ocean.** (A) Distribution of speleothem U-Pb and U-Th ages ( $\pm 2\sigma$ ) in

time and space (details in caption of Fig. 2). (B) Benthic  $\delta^{18}\text{O}$  stack<sup>19</sup> with glacial MIS numbers below and interglacial above; (C) North Atlantic mid-latitude (41°N, 33°W)  $U^{k'}_{37}$  SST as recorded in ODP-607 core<sup>24</sup>, and with a 81 data point (~200 ka) running average showing a  $\approx 3^\circ\text{C}$  decrease in the long-term SST; (D) North Atlantic high-latitude (58°N, 16°W)  $U^{k'}_{37}$  SST as recorded in ODP-982 core<sup>24</sup>, and with 81 data point (~200 ka) running average showing  $\approx 1.5^\circ\text{C}$  decrease in the long-term SST; (E) Percent abundance of genus *Polycopse*, a benthic opportunistic genus signifying high local surface productivity in Arctic sea-ice margin environments, and therefore presence of the sea-ice in Northwind Ridge, western Arctic Ocean<sup>3</sup>.

288

## 289 Methods

### 290 Description of the caves:

#### 291 *Ledyanaya Lenskaya Cave:*

292 The cave is located 116 km E-S-E of the town of Lensk, 180 m above sea level, with the cave entrance  
293 located on the north-eastern riverbank in a cliff ~50 m above the Lena River. The local vegetation is sub-  
294 boreal taiga forest<sup>31</sup>. The cave is developed in Ediacaran limestones and marls and its length is mapped to  
295 ~216 m. A ~90 m long main passage is ascends by ca. 15° in a N-NE direction, ending in a central ~55 m  
296 long and 10-20 m wide hall, with ceiling height up to 8 m. The hall is mostly filled with massive ice several  
297 meters thick. A narrow passage leads from its top to the cave's upper section. The latter is ~70 m long  
298 ascending by ~20°, and consists of two chambers connected by a narrow passage and partly filled by ice.  
299 The walls of these chambers are partly covered by flowstone and stalactites (SLL14, taken in 2014, ED  
300 1A). Ca. 50 m from the main entrance a narrow slightly ascending ~40 m long corridor splits from the main  
301 passage in E-NE direction, and ends in small chambers in which vadose speleothems were collected (SLL9  
302 and SLL10, taken in 2009-2010, ED 1A). The depth of this chamber below the surface is 15-20 m, and the  
303 depth of the large hall is ~60 m.

304 The cave air temperature was monitored using HOBO UA Pendant Temperature Loggers from March  
305 2010 to May 2013 (Logger “Siberia 7”) and November 2013 (Logger “Siberia 6”) (ED 2A, B). The loggers’  
306 measurement uncertainty is  $\pm 0.47^{\circ}\text{C}$ . The temperature in the central hall with massive ice was measured  
307 with logger “Siberia 6” (ED 1A) and was found to vary between  $-0.1^{\circ}\text{C}$  and  $0.0^{\circ}\text{C}$  in early spring, and  
308 between  $+0.6^{\circ}\text{C}$  and  $+0.7^{\circ}\text{C}$  in summer (ED 2A). Logger “Siberia 7” measured the temperature in the  
309 chamber with speleothems SLL9 and SLL10, and the temperature there is relatively stable at  $\sim +0.3^{\circ}\text{C}$  (ED  
310 2A). Although in both places temperatures are slightly above zero, no water seepage or speleothem growth  
311 was found beyond several meters from the entrance, showing that the rock above the cave is frozen year-  
312 round. In the uppermost cave chambers where SLL14 speleothem samples were collected, the temperature  
313 in January 2014 was  $0^{\circ}\text{C}$  and the ice was dry. According to Lensk meteorological station (ED 2B) the mean  
314 annual air temperature (MAAT) between 2010 and 2013 was  $\sim -6^{\circ}\text{C}$ , thus the cave is by  $6^{\circ}\text{C}$  warmer. The  
315 cave’s ascending morphology with the entrance being its topographically lowest point, causes warm humid  
316 air being trapped inside during the summer months. Formation of ice in the uppermost parts of the cave  
317 shows that the cooling that creates the ice occurs when warm and moist air comes in contact with the sub-  
318 zero temperature of the cave walls<sup>32</sup>. This is also supported by the permafrost map, that shows continuous  
319 permafrost (type 18) above the Ledianaya Lenskaya Cave<sup>33</sup> (ED 3A). More information about the cave can  
320 be found in Supplementary Online Materials of Vaks et al (2013)<sup>14</sup>.

321 *Botovskaya Cave:*

322 The cave system is located 58 km N-NE of the town of Zhigalovo, 750 m above sea level, at the head of a  
323 small valley NE of the Boti River, that joins the Lena River 8.6 km SE of the cave. The vegetation is sub-  
324 boreal taiga forest<sup>31</sup>. The cave is located in Ordovician limestones and sandstones, and is the longest cave  
325 system in Russia, reaching a total length of  $>69$  km and depth of up to 130 m below the surface, comprising  
326 a horizontal maze of thousands of passages developed along the crisscross system of tectonic fissures (ED  
327 1B).

328 Cave air temperatures were monitored using HOBO UA Pendant Temp loggers from February 2010 to  
329 February 2016. The temperatures in the deeper parts of the cave are stable at  $+1.9 \pm 0.3^{\circ}\text{C}$  in its but vary  
330 from  $-0.2^{\circ}\text{C}$  to  $+1.6^{\circ}\text{C}$  near the entrance, with minima in winter and maxima in the summer (ED 2C).  
331 Surface air temperatures (SAT) outside the cave were also monitored by a HOBO logger tied on the  
332 northern shady side of a big tree 2 m from the ground. Mean annual SAT is  $-2.1^{\circ}\text{C}$ , varying between summer  
333 and winter extremes from  $+37^{\circ}\text{C}$  to  $<-40^{\circ}\text{C}$  ( $-40^{\circ}\text{C}$  is the minimum limit of the logger; during two nights  
334 in winter 2010-11 the minimum temperature dropped below  $-40^{\circ}\text{C}$ ). MAAT is thus lower than the cave air  
335 temperature by  $3-4^{\circ}\text{C}$  (ED 2D).

336 Regional permafrost is discontinuous and found below the Boti River valley and its slopes, but is absent  
337 from the plateau above the inner parts of Botovskaya Cave<sup>33</sup> (ED 3B). The eastern part of the cave (“New  
338 World”) is where the most water seepage and modern speleothem deposition occurs today (ED 3B). This  
339 cave section is located below a small surface depression that hosts an intermittent stream that allows  
340 rain/snowmelt water to seep into the cave. Thermal energy from infiltrating water probably contributes to  
341 an absence of permafrost in this area. Speleothem samples were collected in the “New World” section of  
342 the cave. The western part of the cave (“Old World”) is drier, with some passages near the entrance clogged  
343 with massive ice.

#### 344 **Speleothem petrography:**

345 In Ledyanaya Lenskaya Cave the speleothem cover on the cave walls and floor is usually 5-10 cm thick.  
346 Speleothems consist of several calcite horizons, each composed of brown or grey columnar calcite  
347 crystals usually clean from detrital material (ED 4, 6A, B). These calcite horizons are separated by  
348 whitish or beige thin ( $<2$  mm) layers of microcrystalline calcite, sometimes containing pieces of marl and  
349 limestone host rock. These layers represent growth hiatuses, sometimes with pieces of broken host rock  
350 from the cave ceiling remaining on the ancient speleothem surface.  
351 In Botovskaya Cave speleothem deposition is much more widespread and massive than in Ledyanaya  
352 Lenskaya Cave. Here the thickness of the speleothems is many tens of cm, showing that compared to

353 Ledyanaya Lenskaya Cave the humid and warmer climate of the area provided speleothems with better  
354 opportunities to grow (ED 5). Active speleothems are also found in this cave. Unlike in Ledyanaya  
355 Lenskaya Cave, most speleothems in Botovskaya Cave are composed of aragonite (ED 6 C, D), but with  
356 some calcite speleothems (e.g. stalagmite SB-6919), and some speleothems comprising alternate aragonite  
357 and calcite layers (e.g. stalagmite SB-01112). Apparent growth breaks, sometimes separating calcite and  
358 aragonite layers, are common.

#### 359 **Methods used in the study**

360 The speleothems were sectioned using a diamond saw. For the purpose of U-Th dating between 10 and 250  
361 mg of powder was drilled from each sampled horizons using 0.8-1 mm drill bits. Speleothem mineralogy  
362 was examined at ETH Zurich, Switzerland, using a Bruker, AXS D8 Advance powder XRD diffractometer,  
363 equipped with a scintillation counter and an automatic sampler. Macro and microscope inspection shows  
364 that all horizons chosen for dating had a typical columnar petrography in calcite and fibrous petrography in  
365 aragonite (ED 6), with almost no voids or re-crystallization marks, suggesting that they likely maintained  
366 closed system conditions for U-series chronology (except for some growth hiatuses, such as that in SB-  
367 01112, ED 5).

#### 368 *U-Pb chronology*

#### 369 *Analytical methodology*

370 Ages were determined by isotope dilution using a mixed  $^{236}\text{U}$ - $^{204}\text{Pb}$ - $^{230}\text{Th}$  spike<sup>34</sup> and a first generation Nu  
371 Plasma MC-ICP-MS. Subsamples were cut using a small diamond saw and transferred to acid-cleaned (1-  
372 2 M  $\text{HNO}_3$  for >3 days) 15 ml polypropylene bottles. The subsamples were then sonicated repeatedly in  
373 18 M $\Omega$ .cm water until no suspended fines were visible, rinsing between each wash. Subsamples were  
374 then twice acid cleaned in distilled 2 %  $\text{HNO}_3$  with sonication to remove any residual dirt. Following each  
375 wash, samples were thoroughly washed with 18 M $\Omega$ .cm water and sonicated to remove any residual acid  
376 and dislodged surface material. Each acid wash was removed before the acid reaction completed, to  
377 prevent adsorption of dissolved ions back on to the surface of the sample.

378

379 One-two drops (~30 µL/drop) of spike were added directly to the acid cleaned carbonate and gently  
380 agitated to mix as the spike fully dissolved the sample. Once visible reaction was complete, the solution  
381 was diluted to ca. 15 ml with 18 MΩ.cm water, thoroughly shaken to homogenise, and then immediately  
382 analysed, with no pre-concentration of U and Pb.

383

384 Analyses followed a six-step routine. In steps 0, 1, 2, and 3,  $^{208}\text{Pb}$ ,  $^{207}\text{Pb}$ ,  $^{206}\text{Pb}$ ,  $^{204}\text{Pb}+^{204}\text{Hg}$  and  $^{202}\text{Hg}$   
385 were measured using three ion-counters at two AMU spacing. The relative gains of the ion-counters were  
386 determined by stepping  $^{204}\text{Pb}+^{204}\text{Hg}$  alternately in to each collector.  $^{202}\text{Hg}$  was monitored to correct for  
387  $^{204}\text{Hg}$  on  $^{204}\text{Pb}$ . In steps 4 and 5  $^{238}\text{U}$  was measured on a Faraday cup, with  $^{235}\text{U}$  and  $^{236}\text{U}$  measured  
388 alternately on both Faraday and ion counter; this allows using the Faraday/Faraday  $^{238}\text{U}/^{235}\text{U}$  ratio, or the  
389 Faraday/ion counter  $^{238}\text{U}/^{235}\text{U}$  ratio depending on  $^{235}\text{U}$  signal intensity. Faraday/Faraday ratios were  
390 normally used for both the  $^{238}\text{U}/^{235}\text{U}$  and the  $^{238}\text{U}/^{236}\text{U}$ .

391

392 Mass fractionation was estimated using the measured  $^{238}\text{U}/^{235}\text{U}$  ratio of the samples and an assumed  
393 natural value 137.75<sup>35</sup>. Based on previous testing of the instrument, the mass fractionation for Pb was  
394 assumed to be 2‰/AMU higher than for U<sup>36</sup>.

395

396 Prior to first analysis, the Nu Instruments DSN100 sample introduction system and sample lines were  
397 cleaned with 10%  $\text{HNO}_3$ , 2%  $\text{HNO}_3$  and 18 MΩ.cm water. A dedicated set of B-type cones reserved for  
398 very low level Pb work were used. These were gently cleaned by rinsing with DI water prior to use to  
399 remove excessive Ca build-up from the skimmer orifice. As far as possible, the surface coating on the  
400 cones was not disturbed. The instrument was then initially tuned and optimised with a 100 ppt Tl solution  
401 and diluted natural U solution. Intentional addition of Pb was avoided during tuning to prevent re-  
402 contamination of the instrument, but sufficient Pb-blank is present in the Tl solution to see the Pb peaks  
403 on the ion counters. Peak shape and optimisation was then re-checked on samples; focusing settings for

the zoom optics often changed substantially from the nominally clean Tl solution to the matrix-heavy samples, especially following cleaning of the cones. Gas flows were also re-optimised to suppress interferences (probably from  $\text{Sr}_2\text{O}_2$ ) which manifest as superimposed peaks  $\sim 0.2$  AMU lighter than the Pb peaks, especially on  $^{208}\text{Pb}$ . Optimisation was checked again after an initial couple of sacrificial analyses and regularly during the analytical session. The DSN100 was re-cleaned with 18 M $\Omega$ .cm water every 1-2 days to remove Ca build-up and U and Pb blank.

Separate sample aliquots up to c. 0.2 g were dissolved and purified to obtain U cuts for measurement of the  $^{234}\text{U}/^{238}\text{U}$  ratio. Purification used 2 ml columns with AG1X8 anion exchange resin. Samples were loaded in, and Ca eluted with c. 10M HCl. U was eluted with 18 M $\Omega$ .cm water. The purified U was measured on the same instrument, with the  $^{234}\text{U}$  and  $^{238}\text{U}$  measured on ion counter and Faraday collectors, respectively. Standard bracketing with CRM145 (CRM112A) was used to correct both for mass fractionation and ion counter gain.

#### Non-radiogenic Pb correction

Model ages were calculated from each pair of U-Pb and  $^{234}\text{U}/^{238}\text{U}$  analyses. The  $^{238}\text{U}$ - $^{206}\text{Pb}$  decay provides the age data used here, but the  $^{235}\text{U}$ - $^{207}\text{Pb}$  system was also measured and provides an assessment of concordance, and thus confidence in obtained ages.

Ages were calculated using an estimated  $^{208}\text{Pb}/^{206}\text{Pb}$  (and  $^{208}\text{Pb}/^{207}\text{Pb}$ ) ratio for the initial non-radiogenic Pb and, the modern-day measured disequilibrium in the  $^{234}\text{U}/^{238}\text{U}$  ratio to constrain the initial  $^{234}\text{U}/^{238}\text{U}$  ratio.  $^{208}\text{Pb}$  is assumed to be entirely non-radiogenic on the basis that the  $^{232}\text{Th}$  is typically at very low concentration in speleothems and that samples are young compared to the  $^{232}\text{Th}$  half-life. Common  $^{208}\text{Pb}/^{206}\text{Pb}$  (and  $^{208}\text{Pb}/^{207}\text{Pb}$ ) for the non-radiogenic Pb correction was estimated by a combination of:



- 1) identifying and analysing unradiogenic parts of the sample, not greatly modified by Pb from decay.
- 2) retrospectively picking approximate isochrons from the data, on the basis that given a large number of analyses the following are likely: a) age overlap between samples/subsamples can be expected and hence some clumping of analyses along mixing lines between the initial Pb composition and the radiogenic composition for a given (approximate) age; b) data should fan around the initial Pb composition; c) subsamples of roughly the same age, can, to a first approximation be grouped based on the observed  $^{234}\text{U}/^{238}\text{U}$  ratio. The latter is somewhat limited by initial  $^{234}\text{U}/^{238}\text{U}$  variation, but surviving  $^{234}\text{U}$  disequilibrium decreases by a factor of 2 for each  $^{234}\text{U}$  half-life, so for a spread of ages over a few hundred ka or more, the variations due to decay of  $^{234}\text{U}$ s will dominate over variations in the initial ratio.
- 3) Linear regressions<sup>35,36</sup> through groups of data of similar age in  $^{234}\text{U}$ (or  $^{238}\text{U}$ )/ $^{206}\text{Pb} - ^{208}\text{Pb}/^{206}\text{Pb}$  isotope space allow an estimate of the initial  $^{208}\text{Pb}/^{206}\text{Pb}$  ratio ( $^{235}\text{U}/^{207}\text{Pb} - ^{208}\text{Pb}/^{207}\text{Pb}$  isotope space for the initial  $^{208}\text{Pb}/^{207}\text{Pb}$  ratio). Only groups containing relatively non-radiogenic analyses (ideally stratigraphically bracketed by more radiogenic analyses) were used, to minimise the effect of incorrectly grouping samples of different age. The groupings used and regression results are shown in Data Table 1 and illustrated in ED 7.

A common  $^{208}\text{Pb}/^{206}\text{Pb}$  ratio of  $1.471 \pm 0.100$  (and  $^{208}\text{Pb}/^{207}\text{Pb}$  ratio of  $2.465 \pm 0.136$ ) (95% confidence) was used for the Ledyanaya Lenskaya Cave samples (ED 7). The former value is based mainly on a single grouping of samples that include the least radiogenic Ledyanaya Lenskaya analysis, but is in agreement with a second generally more radiogenic grouping. All other Ledyanaya Lenskaya data (except data rejected in Data Table 1) are consistent with this common  $^{208}\text{Pb}/^{206}\text{Pb}$  ratio (ED 7).

For Botovskaya Cave samples, which include highly non-radiogenic material, a common  $^{208}\text{Pb}/^{206}\text{Pb}$  ratio of  $1.997 \pm 0.213$  (and  $^{208}\text{Pb}/^{207}\text{Pb}$  ratio of  $2.419 \pm 0.123$ ) (95% confidence) was determined in a similar way.

Formatted: English (United States)

Formatted: English (United States)

Field Code Changed

Field Code Changed

Field Code Changed

Formatted: English (United States)

Formatted: English (United States)

453 As the Botovskaya data also includes some analyses that are almost entirely non-radiogenic, these have  
454 also been taken into account. Sample groupings and regression results are again shown in ED 7 and Data  
455 Table 1.

456  
457 The rather different values of the common Pb composition between the two caves are likely attributable to  
458 host rock composition. Botovskaya and Ledyanaya Lenskaya caves are hosted in rocks of Ordovician and  
459 Late Proterozoic age, respectively, which have had long periods to evolve distinctive Pb compositions  
460 prior to the formation of the speleothems they now host.

461  
462 The use of model ages involves some degree of assumption about the uniformity of the common Pb  
463 composition. Consequently, an indication of the sensitivity of a particular age to the common Pb  
464 correction is given in Data Table 1 and ED 7, and found to be small compared to quoted uncertainties.

465  
466 Pb blanks have not been separately corrected for and are dealt with as part of the total correction for non-  
467 radiogenic Pb. Given that a number of analyses yielded >99% radiogenic  $^{206}\text{Pb}$ , the Pb blank can be  
468 considered a generally minor source of non-radiogenic Pb. Sample  $^{204}\text{Pb}$  was corrected in the isotope  
469 dilution calculation using  $^{208}\text{Pb}$  as a proxy, assuming a natural  $^{208}\text{Pb}/^{204}\text{Pb}$  ratio of  $37.1 \pm 10$  (95%  
470 confidence). For most analyses, >99% of the total  $^{204}\text{Pb}$  originated from the tracer, so the correction is  
471 small.

472  
473 Ages were calculated from the common-Pb-corrected  $^{238}\text{U}/^{206}\text{Pb}$  (and  $^{235}\text{U}/^{207}\text{Pb}$ ) ratio and measured  
474  $^{234}\text{U}/^{238}\text{U}$  ratio using in-house software. Uncertainties were estimated using a Monte Carlo approach.  
475 Initial  $^{230}\text{Th}$  and  $^{231}\text{Pa}$  are assumed to have been absent in the age/concordia calculations. Initial  $^{234}\text{U}$  is  
476 determined based on the present-day  $^{234}\text{U}/^{238}\text{U}$  ratio as part of the age calculation, much as in U-Th  
477 chronology.

478

479 Decay constants used are:  $^{238}\text{U}$ :  $1.55125 \times 10^{-10}$ ,  $^{234}\text{U}$ :  $2.82203 \times 10^{-6}$ ,  $^{230}\text{Th}$ :  $9.17055 \times 10^{-6}$ ,  $^{226}\text{Ra}$ :  
480  $4.33488 \times 10^{-4}$ ,  $^{235}\text{U}$ :  $9.8485 \times 10^{-10}$ ,  $^{231}\text{Pa}$ :  $2.11583 \times 10^{-5}$ ,  $^{232}\text{Th}$ :  $4.9475 \times 10^{-11}$  <sup>18,37,38</sup>.

481 As a cross-check on this methodology, two layers of stalagmite SLL10-6, G and F, were also analyzed  
482 following the method of Mason et al. (2013)<sup>34</sup> involving chemical purification of Pb from subsamples to  
483 generate isochron ages. Within uncertainty, these agree with the analyses obtained with the simplified  
484 protocol outlined above. U-Pb ages were also cross-checked against U-Th ages determined for the parts of  
485 the samples <0.5 Ma old (Data Tables 1 and 2, ED 8).

486

#### 487 Screening of data and data quality

##### 488 *Ledyanaya Lenskaya Cave*

489 Of the 59 U-Pb analyses (Data Table 1)  $^{238}\text{U}$ - $^{234}\text{U}$ - $^{206}\text{Pb}$  ages have been included from 52 analyses (ED  
490 8A). Of the excluded analyses, one has no corresponding  $^{234}\text{U}/^{238}\text{U}$  measurement (SLL10-4-B bottom), so  
491 an age cannot be calculated. Three analyses (two from SLL10-6-B and one from SLL10-6-B/C hiatus) are  
492 non-radiogenic and yield ages with unhelpfully large uncertainties, though usefully help to constrain the  
493 common Pb correction. Two analyses (SLL14-1-C centre and SLL9-1-A2) yield >1.5 Ma apparent ages,  
494 which are not reproduced in other analyses and appear inconsistent with the  $^{234}\text{U}/^{238}\text{U}$  measurements; and  
495 one analysis (SLL10-4-A top) is both out of stratigraphic order and in disagreement with two other  
496 analyses from the same layer.

497

498 The remaining 52 ages are consistently in stratigraphic order. The c. 1.3-1.5 Ma age cluster is useful for  
499 demonstrating analytical robustness, since the common-Pb correction in these analyses is mostly small  
500 and layers can be dated in stratigraphic order with c. 40 ka age resolution, even without pre-concentration  
501 of Pb. The replication of ages of many growth periods between different samples, even where the  
502 magnitude of the common-Pb correction varies substantially, helps to validate the common-Pb value used  
503 to calculate the model ages and corroborates the analytical robustness of the method. The agreement of

the ages for SLL10-6-Ftop and SLL10-6-G with and without pre-concentration of U and Pb should also be noted (ED 8A).

$^{235}\text{U}$ - $^{207}\text{Pb}$  ages are also given for reference in Data Table 1 and are mostly concordant with the  $^{238}\text{U}$ - $^{234}\text{U}$ - $^{206}\text{Pb}$  ages within error (ED 9) (or, in 5 cases, show only slight discordance). These small discordances can probably be attributed to uncertainties in the common Pb correction, and could be accounted for by shifts in the common Pb composition of a few percent.

Samples SLL10-4C, SLL10-5B, SLL10-9A, SLL10-9C and SLL14-1B bottom have notably low  $^{235}\text{U}$ - $^{207}\text{Pb}$  ages relative to their  $^{238}\text{U}$ - $^{234}\text{U}$ - $^{206}\text{Pb}$  ages. None of these  $^{238}\text{U}$ - $^{234}\text{U}$ - $^{206}\text{Pb}$  ages fails on the grounds of being inconsistent with stratigraphic position and they tend to replicate well in other samples (ED 8). It is likely that this discordance is an analytical artefact, specifically incomplete elimination of the molecular interference on  $^{208}\text{Pb}$ . An extraneous contribution on  $^{208}\text{Pb}$  will lead to overcorrection of the common Pb. Since the  $^{207}\text{Pb}$  is typically some 20-30x more sensitive (Data Table 1) to the common Pb correction, a small overcorrection on the  $^{206}\text{Pb}$  can correspond to a significant overcorrection on the  $^{207}\text{Pb}$ , hence the  $^{235}\text{U}$ - $^{207}\text{Pb}$  ages appear anomalously young while the  $^{238}\text{U}$ - $^{234}\text{U}$ - $^{206}\text{Pb}$  ages remain stratigraphically consistent.

The (near-)concordance of the majority of the ages provides confidence in the data from an analytical standpoint.

*Botovskaya Cave <0.7Ma samples*

Of the 13 analyses from Botovskaya Cave, 12  $^{238}\text{U}$ - $^{234}\text{U}$ - $^{206}\text{Pb}$  ages were calculated. The analysis that failed to produce an age was from unradiogenic calcite G layer in SB-01112, which is bracketed between more radiogenic aragonite layers, and so it still useful for constraining the common Pb composition. Ages fall between 0.4 and 0.7 Ma (Data Table 1), and are in stratigraphic order overlapping well with available U-Th ages (ED 8B).  $^{235}\text{U}$ - $^{207}\text{Pb}$  ages could only be calculated for four analyses and are of low precision, but they are all concordant with the  $^{238}\text{U}$ - $^{234}\text{U}$ - $^{206}\text{Pb}$  ages (Data Table 1).

Botovskaya Cave pre- 0.7Ma samples

Botovskaya Cave shows an extensive 2 Ma and older record, which is the subject of ongoing investigation. Data of some of these samples are used to better constrain the common Pb correction in the present work (Data Table 1, ED 7), although the ages are not used here because no pre-0.7 Ma Botovskaya samples overlapping the older part of the Ledyanaya Lenskaya record have yet been identified.

U-Th chronology:

The U and Th analysis, as well as U-Th ages calculations were performed following Vaks et al (2013) SOM<sup>14</sup>. Twelve layers of five samples from Botovskaya Cave were dated. Dating results and their correction for initial Th were calculated using Isoplot 4.15<sup>39</sup> and are presented in Data Table 2. <sup>238</sup>U concentrations in calcite vary between 0.44 to 1.25 ppm, whereas in aragonite they vary from 40.4 to 136.7 ppm. <sup>232</sup>Th concentrations usually vary between 0.06 and 3.15 ppb. <sup>230</sup>Th/<sup>232</sup>Th activity ratios in the analysed samples varied between 6322 to >10<sup>6</sup>, and the <sup>232</sup>Th/<sup>238</sup>U activity ratios varied between 4.78\*10<sup>-4</sup> and 8.94\*10<sup>-7</sup>. Thus, correction for Th<sub>initial</sub> was negligible. Two ages from layer SB-01112-D were rejected because this layer is adjacent to a horizon with high porosity, representing a joint between a growth hiatus and a crack in the speleothem. The lower part of layer “SB-01112-D bottom” shows an age reversal, possibly due to U leaching. Other U-Th ages shown in ED 4, 5, 8 are taken from Vaks et al (2013)<sup>14</sup>, slightly modified using updated half-lives of <sup>234</sup>U and <sup>230</sup>Th<sup>18</sup>.

The ability of Arctic air to reach Ledyanaya Lenskaya Cave site

Arctic air masses bring polar air southward to substantially influence Siberian weather. In particular, these air masses are capable of bringing latent heat and moisture from still unfrozen Arctic Ocean into Siberian continental interior during the period of October-early November. During this time of the year the Arctic Ocean is still partly unfrozen and snow cover is forming over the Siberian landmass. To demonstrate that these incursions of Arctic air are capable of reaching the site of Ledyanaya Lenskaya Cave, we show on ED10 figure twelve examples of such snow events above Ledyanaya Lenskaya Cave. Three trajectories for air on elevations 500, 1500 and 5000m were calculated for each event with at least one trajectory in each

553 event starts in Arctic Ocean. These trajectories were assessed using the NOAA Hysplit program  
 554 (<https://ready.arl.noaa.gov/HYSPLIT.php>)<sup>40,41</sup>. The proper timing of the weather events mentioned above  
 555 was received from log data of Lensk meteorological station (number 24923), 139 km NW from Ledyanaya  
 556 Lenskaya Cave ([https://rp5.ru/Погода в Ленске, Республика Саха \(Якутия\)](https://rp5.ru/Погода в Ленске, Республика Саха (Якутия))) (in Russian)<sup>42</sup>).

# 557 Methods References:

- 558 31 Tchebakova, N. M., Rehfeldt, G. E. & Parfenova, E. I. in *Permafrost Ecosystems. Ecological*  
 559 *Studies (Analysis and Synthesis)* Vol. 209 (eds Osawa A. et al.) 427-446 (Springer, 2010).
- 560 32 Ford, D. & Williams, P. W. *Karst Geomorphology and Hydrology*. (Unwin Hyman, 1989).
- 561 33 Seligman, B. *The English language edition of the geocryological map of Russia and neighbouring*  
 562 *republics. P.J. Williams and I.M.T. Warren. 1999. Ottawa: Collaborative Map Project. Handbook:*  
 563 *32 p, soft cover. ISBN 0-9685013-0-3. Map: 16 sheets (95 × 66 cm per sheet), scale 1:2,500,000.*  
 564 *\$US350.00. 2009/10/27 edn, Vol. 36 (Cambridge University Press, 2000).*
- 565 34 Mason, A. J., Henderson, G. M. & Vaks, A. An Acetic Acid-Based Extraction Protocol for the  
 566 Recovery of U, Th and Pb from Calcium Carbonates for U-(Th)-Pb Geochronology. *Geostandards*  
 567 *and Geoanalytical Research* **37**, 261-275, doi:10.1111/j.1751-908X.2013.00219.x (2013).
- 568 35 Hiess, J., Condon, D. J., McLean, N. & Noble, S. R. <sup>238</sup>U/<sup>235</sup>U Systematics in Terrestrial Uranium-  
 569 Bearing Minerals. *Science* **335**, 1610-1614, doi:10.1126/science.1215507 (2012).
- 570 36 Mason, A. J. & Henderson, G. M. Correction of multi-collector-ICP-MS instrumental biases in  
 571 high-precision uranium-thorium chronology. *International Journal of Mass Spectrometry* **295**,  
 572 26-35 (2010).
- 573 37 Cheng, H., Edwards, R. L., Murrell, M. T. & Benjamin, T. M. Uranium-thorium-protactinium  
 574 dating systematics. *Geochimica et Cosmochimica Acta* **62**, 3437-3452,  
 575 doi:[https://doi.org/10.1016/S0016-7037\(98\)00255-5](https://doi.org/10.1016/S0016-7037(98)00255-5) (1998).
- 576 38 Steiger, R. H. & Jäger, E. Subcommission on geochronology: Convention on the use of decay  
 577 constants in geo- and cosmochemistry. *Earth and Planetary Science Letters* **36**, 359-362,  
 578 doi:[https://doi.org/10.1016/0012-821X\(77\)90060-7](https://doi.org/10.1016/0012-821X(77)90060-7) (1977).
- 579 39 Ludwig, K. A. in *Berkeley Geochronological Centre, Special Publication* Vol. 5 (ed Kenneth A.  
 580 Ludwig) (Berkeley Geochronological Centre, Berkeley CA, USA, 2012).
- 581 40 Rolph, G., Stein, A. & Stunder, B. Real-time Environmental Applications and Display sYstem:  
 582 READY. *Environmental Modelling & Software* **95**, 210-228,  
 583 doi:<https://doi.org/10.1016/j.envsoft.2017.06.025> (2017).
- 584 41 Stein, A. F. et al. NOAA's HYSPLIT Atmospheric Transport and Dispersion Modeling System.  
 585 *Bulletin of the American Meteorological Society* **96**, 2059-2077, doi:10.1175/bams-d-14-00110.1  
 586 (2015).
- 587 42 Bulygina, O. N., Veselov, V. M., Razuvaev, V. N. & Aleksandrova, T. M. DESCRIPTION OF HOURLY  
 588 DATA SET OF METEOROLOGICAL PARAMETERS OBTAINED AT RUSSIAN STATIONS,  
 589 <http://meteo.ru/english/climate/descrip12.htm>, [http://meteo.ru/english/climate/cl\\_data.php](http://meteo.ru/english/climate/cl_data.php).  
 590 (2014).

591

# 592 Corresponding author:

593 Anton Vaks, [antonv@gsi.gov.il](mailto:antonv@gsi.gov.il)

594 **Competing interests:**

595 The authors declare no competing interests.

596 **Data availability statement:**

597 The chronology data from this article is available on NGDC database: Vaks, A. (2019): Speleothem  
598 chronology in Ledyanaya Lenskaya and Botovskaya caves used in publication "Paleoclimate evidence of  
599 vulnerable permafrost during times of low sea-ice" By Vaks, A. et al. 2019. British Geological Survey.  
600 (Dataset). <https://dx.doi.org/10.5285/d56addfe-b7b8-4b70-9617-fadc1f7666b4>

601 All data that support the findings of this study are available from the corresponding author on request as  
602 well.

603

604 **Extended Data 1: Caves' maps.** A) Map and cross-section of Ledyanaya Lenskaya Cave, with speleothem  
605 and temperature logger positions; B) Map of Botovskaya Cave with locations of speleothems and  
606 temperature loggers.

607

608 **Extended Data 2: Temperature data inside and outside caves.** A) Ledyanaya Lenskaya Cave air  
609 temperatures between March 2010 and December 2013; B) Comparison of air temperature in Ledyanaya  
610 Lenskaya Cave (from panel A), mean annual surface temperature and surface air temperature changes  
611 (Lensk meteorological station 24923 data); C) Monitoring of air temperatures inside Botovskaya Cave  
612 (February 2010 - February 2016); Between 2010 and 2014 temperatures were monitored deep inside the  
613 cave, whereas between 2015 and 2016 loggers were placed closer to the entrance; D) Comparison of  
614 Botovskaya Cave temperatures with mean surface temperature and surface temperature changes between  
615 February 2010 and July 2014 (data from temperature logger outside the cave).

616

617 **Extended Data 3: Detailed permafrost maps.** A) Permafrost map of the Ledyanaya Lenskaya Cave area<sup>33</sup>,  
618 the cave site is marked by a magenta circle. Lensk and Olekminsk are marked by black circles. B)  
619 Permafrost map of the Botovskaya Cave area<sup>33</sup>, the cave location is marked by magenta circle. Zhigalovo  
620 is marked by black circle. Types and thickness of the permafrost are shown below. In places with continuous  
621 permafrost (types 18-20), it covers >95% of the area, but may contain small unfrozen units (taliks), mainly  
622 under permanent bodies of water. Taliks may go through the entire permafrost layer (through taliks), or  
623 through part of it (not through taliks).

624

625 **Extended Data 4: Pictures of speleothems' cross-sections with ages (in ka) from Ledyanaya**  
626 **Lenskaya Cave.** Age uncertainties are  $2\sigma$ . The U-Pb ages shown in black and a single U-Th age in  
627 stalactite SLL9-2<sup>14</sup> is shown in brown. Hiatuses are shown with red arrows. All speleothems are  
628 composed of calcite.

629

630 **Extended Data 5: Pictures of speleothems' cross-sections with ages (in ka) from Botovskaya Cave.**  
631 Age uncertainties are  $2\sigma$ . The U-Pb ages shown in black and U-Th ages<sup>14</sup> are shown in brown. Most  
632 speleothems are composed of aragonite, except stalagmite SB-6919, and layers A-D, G in stalagmite SB-  
633 01112 which are calcitic.

634

635 **Extended Data 6: Speleothems' petrography.** A) Calcitic stalagmite SLL10-6 with its layered structure;  
636 B) Magnified area (5 to 3 mm - rectangle on the top of A) in crossed polar light, showing columnar crystals;  
637 C) Aragonitic stalagmite SB-7497(3) with fibrous crystals; D) Magnified area (3 to 1.5 cm) shown by black  
638 rectangle in C in plain polar light.

639



640 **Extended Data 7: Common Pb composition assessment for Ledyanaya Lenskaya (upper) and**  
 641 **Botovskaya (lower) caves.**  $^{234}\text{U}$ - $^{206}\text{Pb}$  and  $^{238}\text{U}$ - $^{206}\text{Pb}$  appear on the left, and  $^{235}\text{U}$ - $^{207}\text{Pb}$  on the right, showing  
 642 consistent common Pb values for each cave. The y-intercept represents the common lead ratio, yellow bars  
 643 show the assigned range for common Pb in age calculations. Groups refer to the regression groups in Data  
 644 Table 1 with solid black lines showing regression fits. Grey contours show the percentage change in  
 645 calculated age resulting from changing the common Pb composition by its assigned uncertainty. Dashed  
 646 black lines show reference isochrons and ungrouped data is shown by grey circles. Uncertainties ( $2\sigma$ ) are  
 647 sometimes smaller than the symbol size. Particular details for each plot:  
  
 648 A) Estimate of the common  $^{208}\text{Pb}/^{206}\text{Pb}$  for Ledyanaya Lenskaya Cave in  $^{234}\text{U}/^{206}\text{Pb}$ -  $^{208}\text{Pb}/^{206}\text{Pb}$  isotope  
 649 space.  $^{234}\text{U}$  is used in the plot instead of  $^{238}\text{U}$  to suppress scatter in the  $\text{U}/^{206}\text{Pb}$  ratio due to variations in the  
 650  $^{234}\text{U}/^{238}\text{U}_{\text{initial}}$  ratio. All but two of the ungrouped data have age uncertainties due to common Pb of  $<1\%$  and  
 651 are thus insensitive to the common Pb correction. Most data that are more sensitive to the common Pb  
 652 composition (i.e. those between the 1% and 3% contours) are included in the regressions to estimate the  
 653 common Pb composition.  
  
 654 B) Equivalent plot in  $^{235}\text{U}/^{207}\text{Pb}$ - $^{208}\text{Pb}/^{207}\text{Pb}$  isotope space for the estimation of the common  $^{208}\text{Pb}/^{207}\text{Pb}$   
 655 ratio for Ledyanaya Lenskaya cave. Group 3 and 4 correspond to the clump of ungrouped data close to the  
 656 horizontal axis at c. 0.225 on plot A. Note that  $^{235}\text{U}/^{207}\text{Pb}$  ages are substantially more sensitive to the  
 657 common Pb correction; these ages are used as a check on U-Pb concordance rather than to derive the dates  
 658 used in the paper.  
  
 659 C) Estimate of the common  $^{208}\text{Pb}/^{206}\text{Pb}$  for Botovskaya Cave in  $^{238}\text{U}/^{206}\text{Pb}$ -  $^{208}\text{Pb}/^{206}\text{Pb}$  isotope space.  
 660 Groups 1, 3, 4 and 6 (plotted as squares) are unpublished data from c. 2 Ma samples included here only to  
 661 provide additional constraint on the common Pb composition (Data Table 1). Ages used here are from the  
 662 data plotted as circles. As for Ledyanaya Lenskaya Cave, the common Pb estimate includes the data for  
 663 which the correction matters most as far as is possible.

664 D) Equivalent plot in  $^{235}\text{U}/^{207}\text{Pb}$ - $^{208}\text{Pb}/^{207}\text{Pb}$  isotope space for the estimation of the common  $^{208}\text{Pb}/^{207}\text{Pb}$  ratio  
665 for Botovskaya Cave.  $^{235}\text{U}/^{207}\text{Pb}$  data are more sensitive to the common Pb correction.

666

667 **Extended Data 8: Detailed speleothems' chronologies.** A) The chronology of Ledyanaya Lenskaya Cave  
668 speleothems with 95% confidence errors. Each column in the plot represents one individual speleothem  
669 named in bottom horizontal axis. In each column, the U-Pb ages (purple circles) appear in stratigraphic  
670 order from left (young) to right (old). For each U-Pb age the corresponding proportion of radiogenic  $^{206}\text{Pb}$   
671 (right vertical axis) is shown by red circles above. The U-Th age of the youngest layer A in the stalactite  
672 SLL9-2<sup>14</sup> is shown by blue circle (bottom-left). The two isochron ages of layers Ftop and G in SLL10-6  
673 stalagmite are shown by olive circles. Several replicate age determinations for similar layers were  
674 performed and appear in the plot in the same order as shown in Data Table 1; B) Botovskaya Cave  
675 speleothems' U-Th ages (dark blue circles, left Y axis, Vaks et al, 2013<sup>14</sup> and current work) and U-Pb ages  
676 (light blue circles, left Y axis), the latter are given with percentages of radiogenic  $^{206}\text{Pb}$  (red circles, right Y  
677 axis). All age uncertainties are shown by 95% confidence error bars. The stratigraphic age of the layers  
678 dated from stalagmite SB-01112 increases from left to right.

679

680 **Extended Data 9:  $^{238}\text{U}$ - $^{234}\text{U}$ - $^{206}\text{Pb}$  ages and concordance of  $^{235}\text{U}$ - $^{207}\text{Pb}$  ages for Ledyanaya Lenskaya**  
681 **Cave** (based on Data Table 1). Ages and age uncertainties are shown in black with the corresponding  
682 coloured error bar indicating the degree of concordance ( $^{235}\text{U}$ - $^{207}\text{Pb}$  age as a percentage of the  $^{238}\text{U}$ - $^{234}\text{U}$ -  
683  $^{206}\text{Pb}$  age; blue horizontal line indicates perfect concordance) of the  $^{235}\text{U}$ - $^{207}\text{Pb}$  age. Blue error bars indicate  
684 the analysis is concordant within error. Orange error bars denote slightly discordant analyses, where the  
685 apparent discordance is likely due to common Pb correction on  $^{207}\text{Pb}$ . Red error bars denote analyses that  
686 are discordant with markedly low  $^{235}\text{U}$ - $^{207}\text{Pb}$  ages attributed to overcorrection of the common Pb due to a  
687 residual interference on  $^{208}\text{Pb}$ . The numbers and bars in red show the percentage bias in the  $^{238}\text{U}$ - $^{234}\text{U}$ - $^{206}\text{Pb}$   
688 ages if the discordance of these samples is attributed to an interference on  $^{208}\text{Pb}$ , based on the relative

sensitivity of the  $^{235}\text{U}$ - $^{207}\text{Pb}$  and  $^{238}\text{U}$ - $^{234}\text{U}$ - $^{206}\text{Pb}$  ages to the common Pb correction (Data Table 1). Grey horizontal lines indicate where ages replicate in two or more speleothems. The biases in the  $^{238}\text{U}$ - $^{234}\text{U}$ - $^{206}\text{Pb}$  ages attributed to the interference on  $^{208}\text{Pb}$  do not change these ages outside of error, hence, the tendency of these ages to replicate well in other samples. The discordance arises almost entirely from the  $^{235}\text{U}$ - $^{207}\text{Pb}$  ages (which are not used), due to their vastly greater sensitivity to over-correction of the common Pb than the  $^{238}\text{U}$ - $^{234}\text{U}$ - $^{206}\text{Pb}$  ages. Errors are 95% confidence. For each speleothem, the stratigraphic age of the dated layers increases from left to right.

696

**Extended Data 10: HYSPLIT-model-based 7 day back-trajectories of 12 snow events in Ledyanaya**

**Lenskaya Cave site.** These snowfall events were accompanied by significant decrease in air temperature indicating that Arctic air was involved in the synoptic event. Six snow events occurred in October and first half of November 2012 (A – F), and other six events occurred in October and first half of November of 2013 (G – L). For each of 12 events, three back trajectories for elevations of 500, 1500 and 5000 m above sea level were calculated, with at least one of them originating in Arctic Ocean in each case. The dates and times of the events are as follows: A – 04/10/2012, 21:00; B – 07/10/2012, 21:00; C – 19/10/2012, 09:00; D – 21/10/2012, 15:00; E – 05/11/2012, 09:00; F – 11/11/2012, 09:00; G – 01/10/2013, 09:00; H – 09/10/2013, 00:00; I – 19/10/2013, 09:00; J – 25/10/2013, 09:00; K – 02/11/2013, 09:00; L – 10/11/2013, 09:00.

Identification information:

A – Job ID: 164576, Job Start: Tue 3 Sep, 12:19:42, UTC 2019; Meteorology: 0000Z, 1 Oct 2012 – GDAS1;

B – Job ID: 165119; Job Start: Tue 3 Sep, 12:46:49, UTC 2019; Meteorology: 0000Z, 1 Oct 2012 – GDAS1;

712 C – Job ID: 169518, Job Start: Sun 8 Sep 14:04:06, UTC 2019; Meteorology: 0000Z, 15 Oct 2012 –  
713 GDAS1;

714 D – Job ID: 169478, Job Start: Sun 8 Sep 13:58:40, UTC 2019; Meteorology: 0000Z, 22 Oct 2012 –  
715 GDAS1;

716 E – Job ID: 171083 , Job Start: Sun 8 Sep 15:42:40, UTC 2019; Meteorology: 0000Z, 1Nov 2012 –  
717 GDAS1;

718 F – Job ID: 171195, Job Start: Sun 8 Sep 15:47:51, UTC 2019; Meteorology: 0000Z, 8 Nov 2012 –  
719 GDAS1;

720 G – Job ID: 187728, Job Start: Fri 30 Aug 12:07:03 UTC 2019; Meteorology: 0000Z, 1 Oct 2013 –  
721 GDAS1;

722 H – Job ID: 172040, Job Start: Sun 8 Sep 16:46:37 UTC 2019; Meteorology: 0000Z, 8 Oct 2013 –  
723 GDAS1;

724 I – Job ID: 172169, Job Start: Sun 8 Sep 16:54:44 UTC 2019; Meteorology: 0000Z, 15 Oct 2013 –  
725 GDAS1;

726 J – Job ID: 172846, Job Start: Sun 8 Sep 17:16:55 UTC 2019; Meteorology: 0000Z, 22 Oct 2013 –  
727 GDAS1;

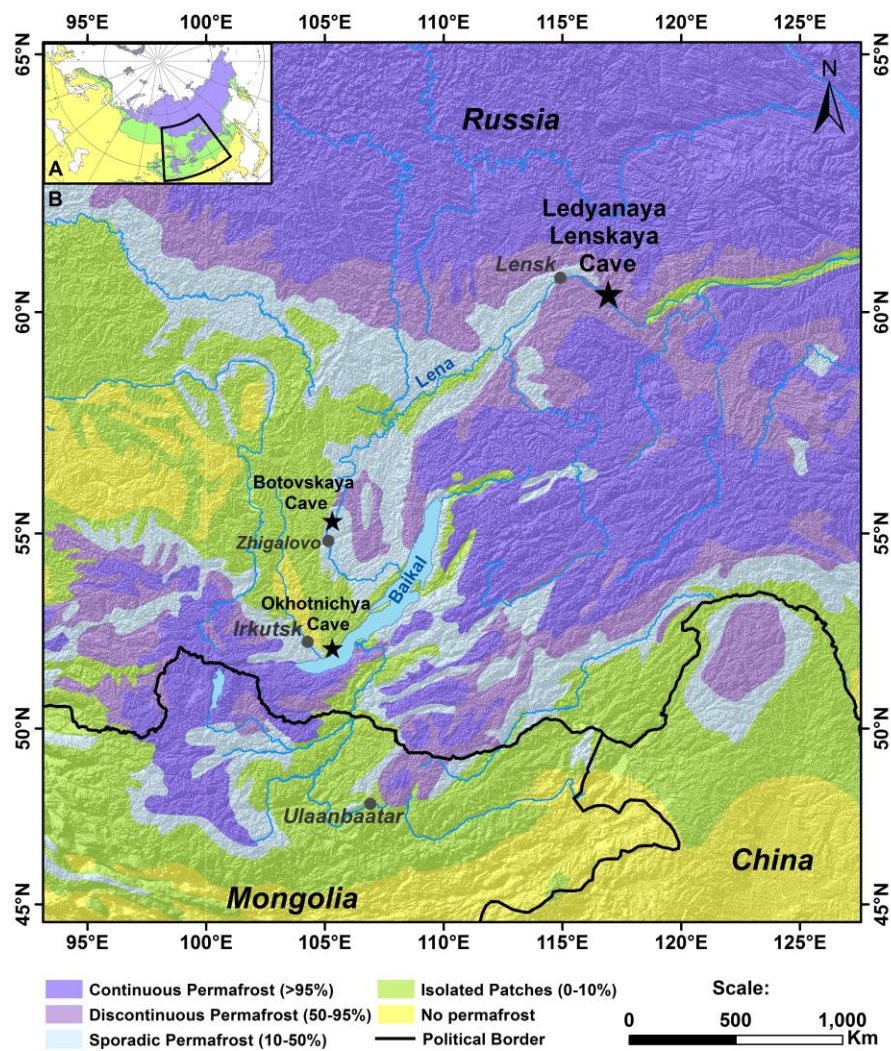
728 K – Job ID: 173152, Job Start: Sun 8 Sep 17:24:37 UTC 2019; Meteorology: 0000Z, 1 Nov 2013 –  
729 GDAS1;

730 L – Job ID: 173482, Job Start: Sun 8 Sep 17:32:06 UTC 2019; Meteorology: 0000Z, 8 Nov 2013 –  
731 GDAS1.

732 Parameters equal for all calculations in ED10:

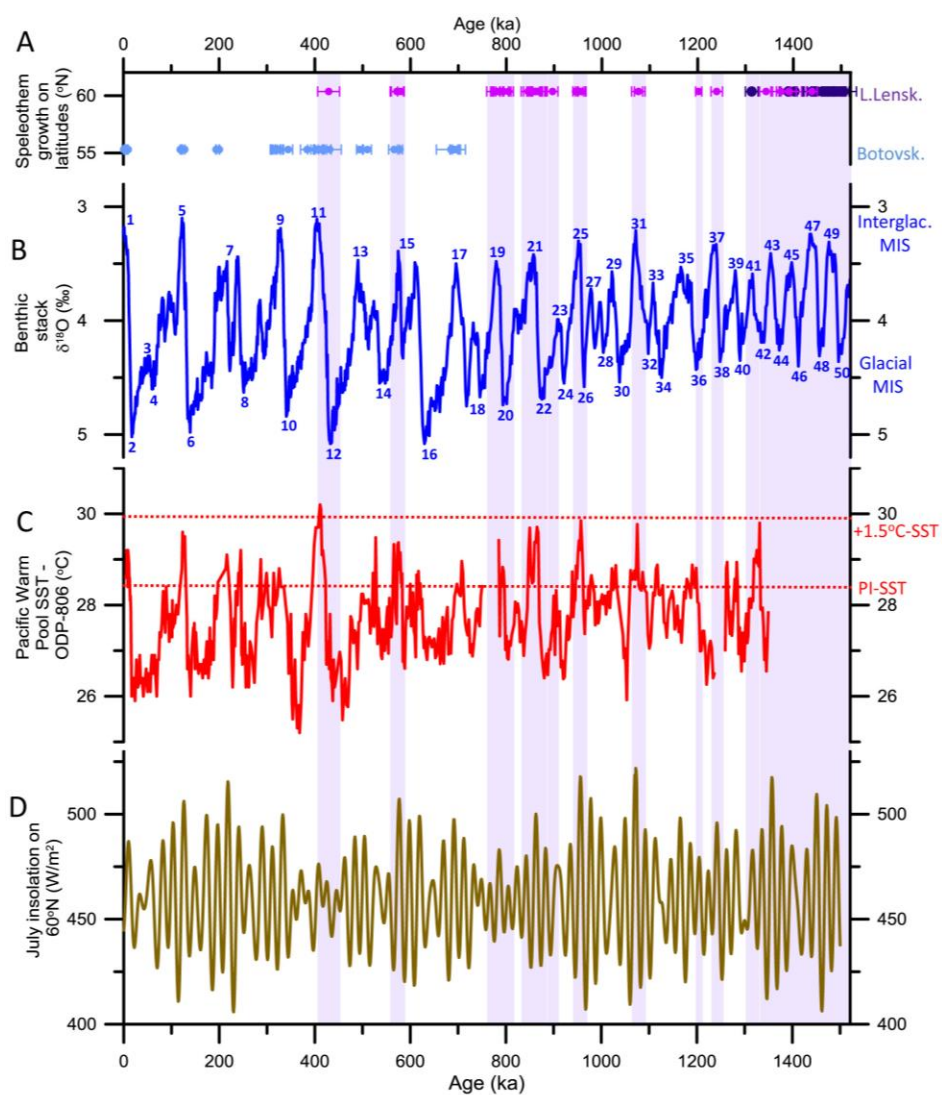
733 Source: Lat. 60.371000, Long. 116.946472; Hights: 500 m, 1500 m, 5000 m AGL; Trajectory direction:  
734 Backward; Duration: 168 hrs; Vertical Motion Calculation Method: Model Vertical Velocity.

735 **Figure 1:**

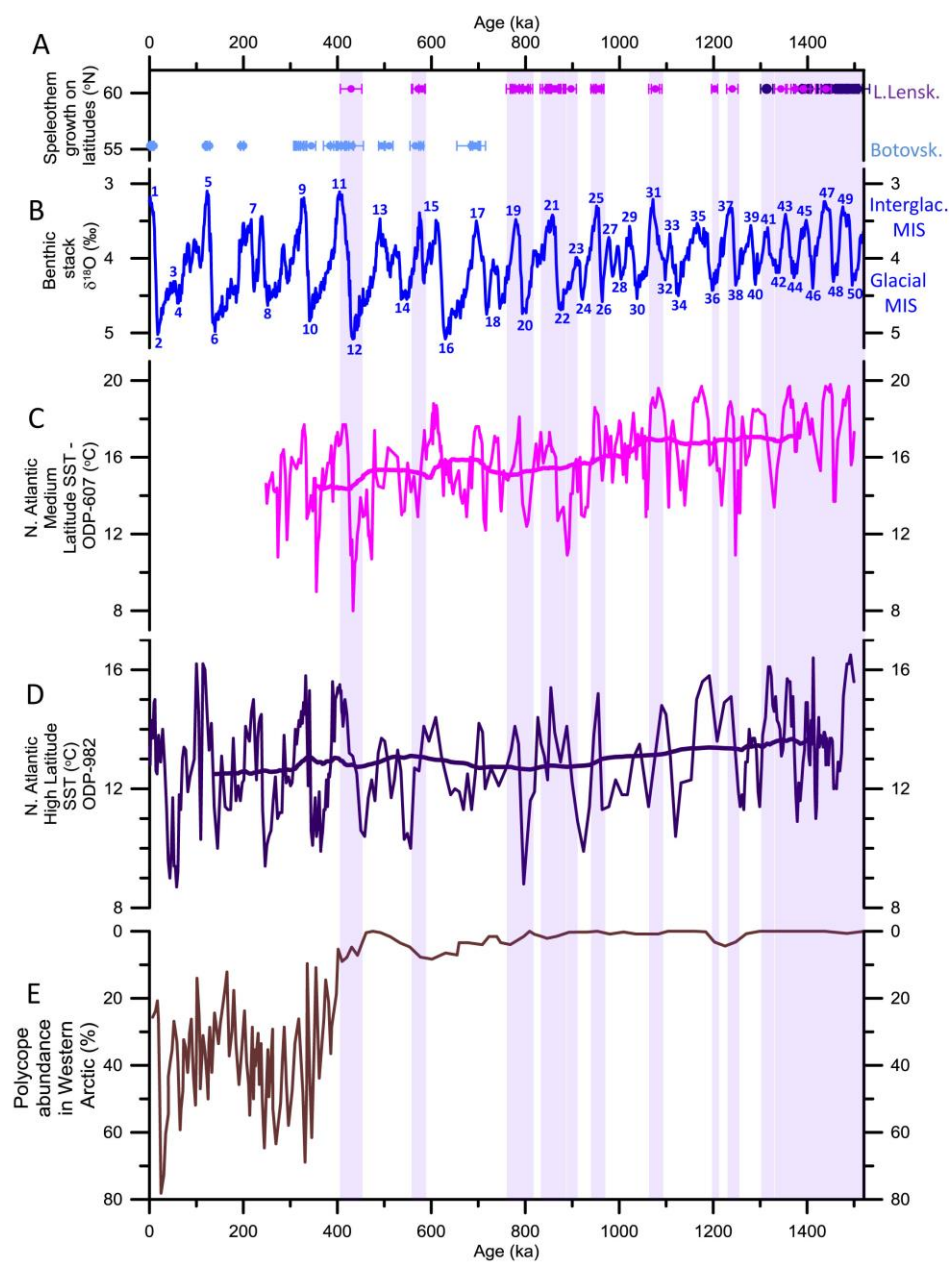


736

737 **Figure 2:**



741 **Figure 3:**



742